On measures of mechanical behaviour*

P. RAMA RAO
Jawaharlal Nehru Centre for Advanced Scientific Research, Bangalore 560 064.

Abstract

Strength and fracture properties are commonly determined by carrying out standardized tension and toughness tests. Engineering structures and components experience a more complex mechanical environment in terms of stress state, rate and extent of deformation. Considering three such situations, namely, erosive wear, ballistic penetration and low cycle fatigue, it is suggested that mechanical energy density obtained from tests that simulate the application environment correlates better with mechanical performance.

Keywords: Mechanical energy density, erosive wear, ballistic penetration, low cycle fatigue.

1. Introduction

Engineering structures and components are invariably subject to elastic deformation and inevitably undergo plastic deformation in several service situations. In the case of elastic deformation, the yield strength of the material (σ_{YS}) is the dominant design parameter and $\sigma_{YS}^2/2E$, where E, the elastic modulus of the material, represents, per unit volume, the *limiting* energy absorption capability of the material and is termed the modulus of resilience. When a structural element is subject to plastic deformation, the energy absorption capability per unit volume of the material is defined in terms of the product of true plastic stress and true plastic strain experienced. This product is referred to as the mechanical energy density (MED). Unlike in the case of elastic deformation, the energy absorbed by a material through plastic deformation, *i.e.*, MED, is essentially dissipated as heat with only a small fraction (<2%) being stored in the material in the form of defects.

While for elastic deformation the modulus of resilience defines a limiting energy absorption capability, a limiting energy absorption capability of a material in the plastic deformation regime cannot be defined in a unique manner. Consider a tensile test wherein the sample is pulled with increasing load and at a constant cross-head speed till it fractures. A typical stress–strain curve from such a test is presented in Fig. 1. In this figure, the various strength and ductility parameters usually obtainable from a tensile test are illustrated. The area under the stress–strain curve (*i.e.*, area OABCD) is the mechanical energy density. In this case, MED is limited by the formation of the neck in the sample (neck starts forming at around point B) and subsequent fracture (points C and D) along the neck. In contrast, if a compression test is carried out on the same test material
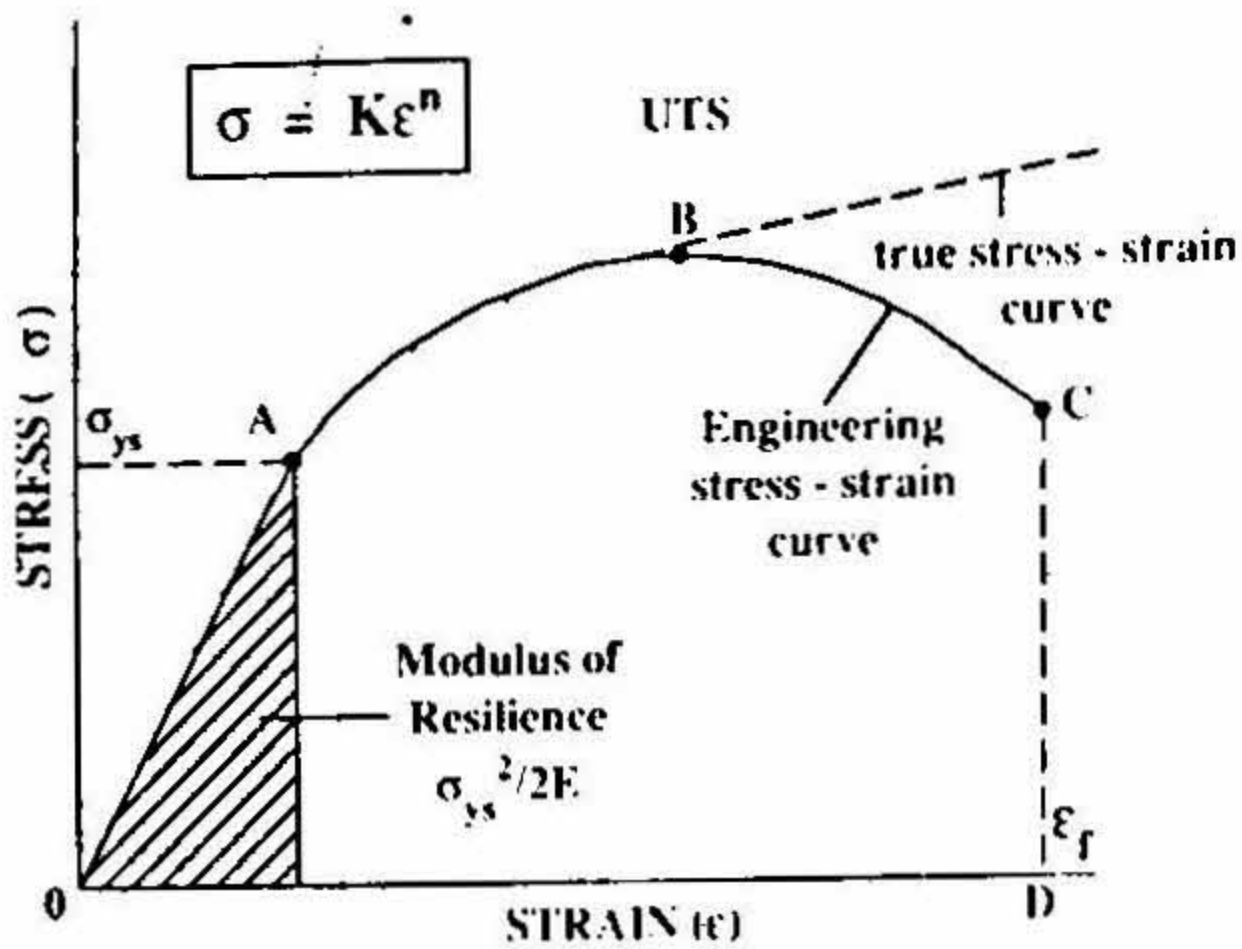
FIG. 1. Schematic diagram of a typical flow stress–strain curve as obtained from a tensile test.

the plastic deformation continues up to very large strains (as high as 1000% in carefully conducted tests) without fracture. Thus, the MED for the same material under compression test conditions is substantially larger than the MED under tensile test conditions (Fig. 1).

From the simple picture described above, an important conclusion that emerges is that, unlike the thermophysical properties like the elastic modulus, density, specific heat and melting point, the parameter MED for a material is not a unique property and depends on the environment that includes stress state, rate and extent of deformation encountered by it during its service.

Various deformation processes that a given material may witness during its application can be illustrated, in perspective, in a strain rate–plastic strain space. (Fig. 2). Evidently, erosion and ballistic penetration are characterized by material deformation at ultra-high strain rates and moderate strains. In contrast, abrasion induces very large strains in the material getting abraded. Large strains are also encountered by a material undergoing low cyclic fatigue. However, in this case, such an accumulation of strain occurs under cyclic straining conditions.

The main objective of this paper is to illustrate through a consideration of a few varied mechanical environment situations that parameters obtainable from conventional tests, such as the tensile test, including MED, cannot be used to correlate with mechanical behaviour under complex loading conditions. If so what material parameter can the engineer rely on? The answer seems to lie in the evaluation of MED under conditions *simulating* its intended application. For this purpose, in this paper, three material degradation mechanisms, namely, erosion, ballistic penetration and high strain fatigue have been chosen. Their choice is dictated by the fact that they are characterised by a mechanical environment substantially different from that of the simple and commonly used tensile test.

2. Erosive wear

Erosive wear involves the removal of material from component surfaces by repeated impacts of hard, angular particles travelling at considerable impact velocities (10 to 300 m/s)[1,2]. Erosive wear is a dominant material degradation mechanism encountered by
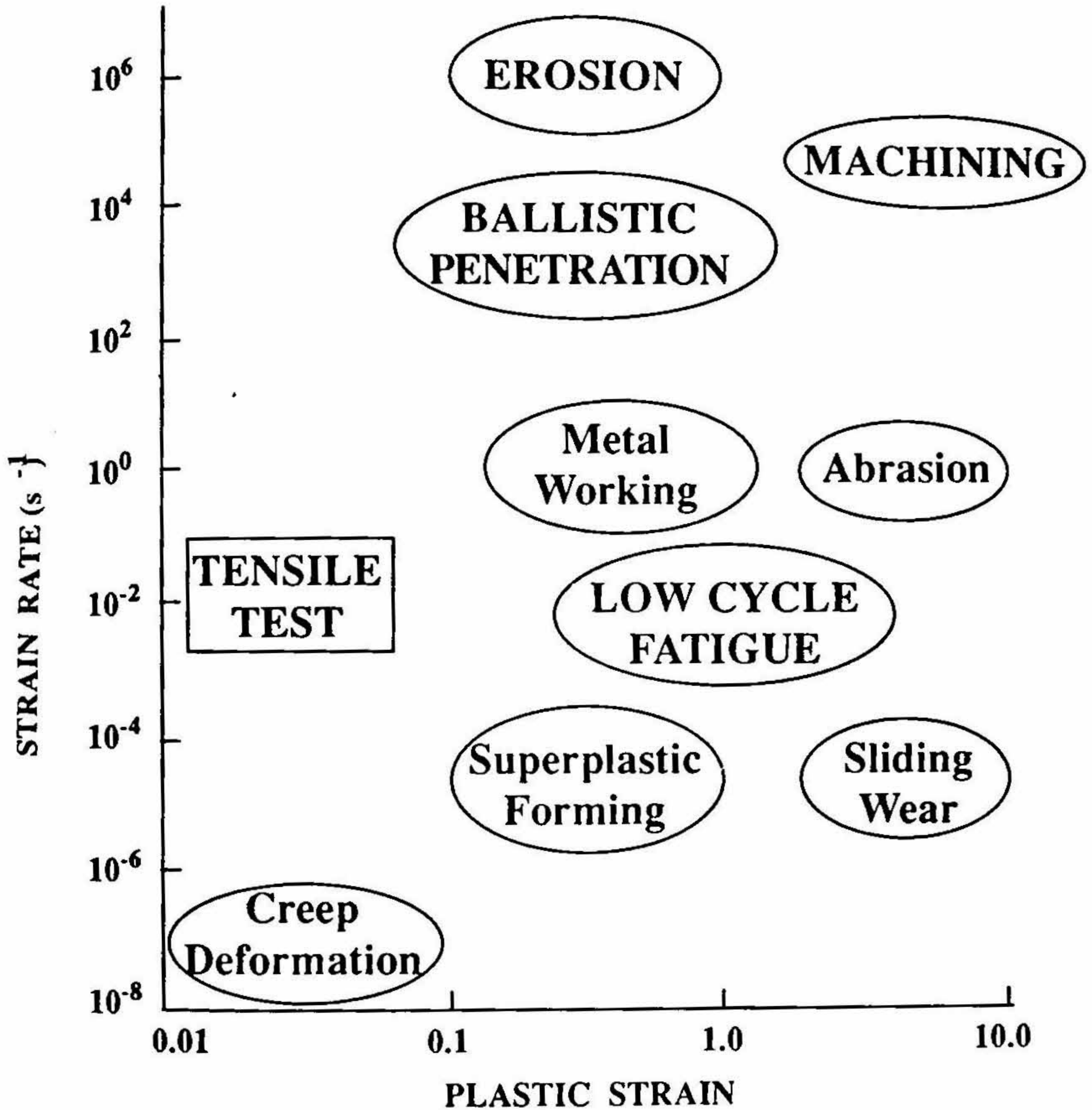
FIG. 2. Regime of various mechanical degradation processes in the axes of plastic strain rate and plastic strain.

various components in the gas turbine engines of aircraft and land-based gas turbine power stations, thermal power plants, pneumatic solid/slurry conveyor systems and coal gasification/liquefaction plants[3, 4].

During erosion, the erodent particles impact and indent the component surface to form craters and in the process form lips all around the crater periphery. Figure 3 represents the SEM photograph of a typical eroded surface. The lips, protruding out of the original component surface, get removed during subsequent impacts by the erodent particles. The removal of material at the micro-level on a continuous basis as described above causes the 'thinning' of the component (e.g., reduction in wall thickness) and, more importantly,
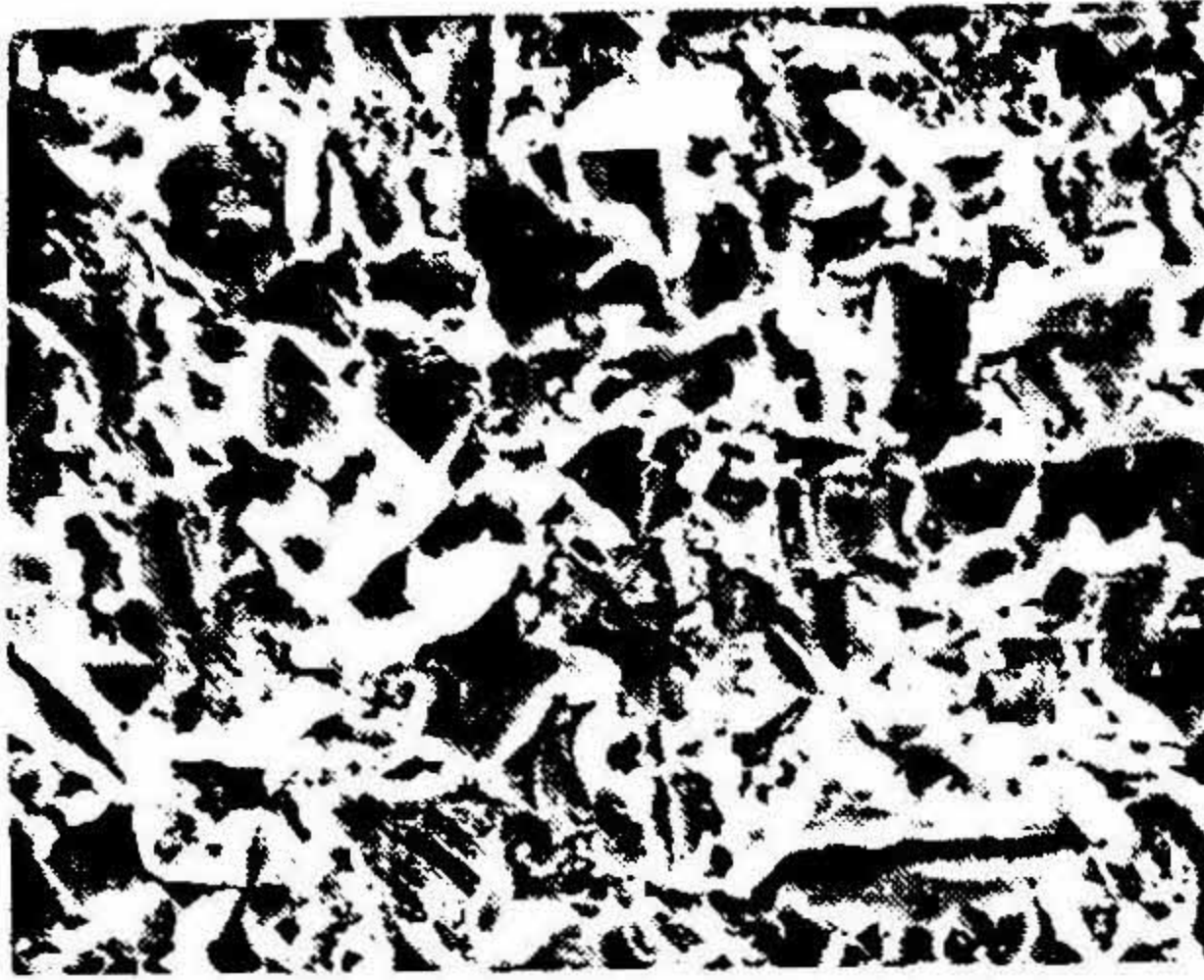
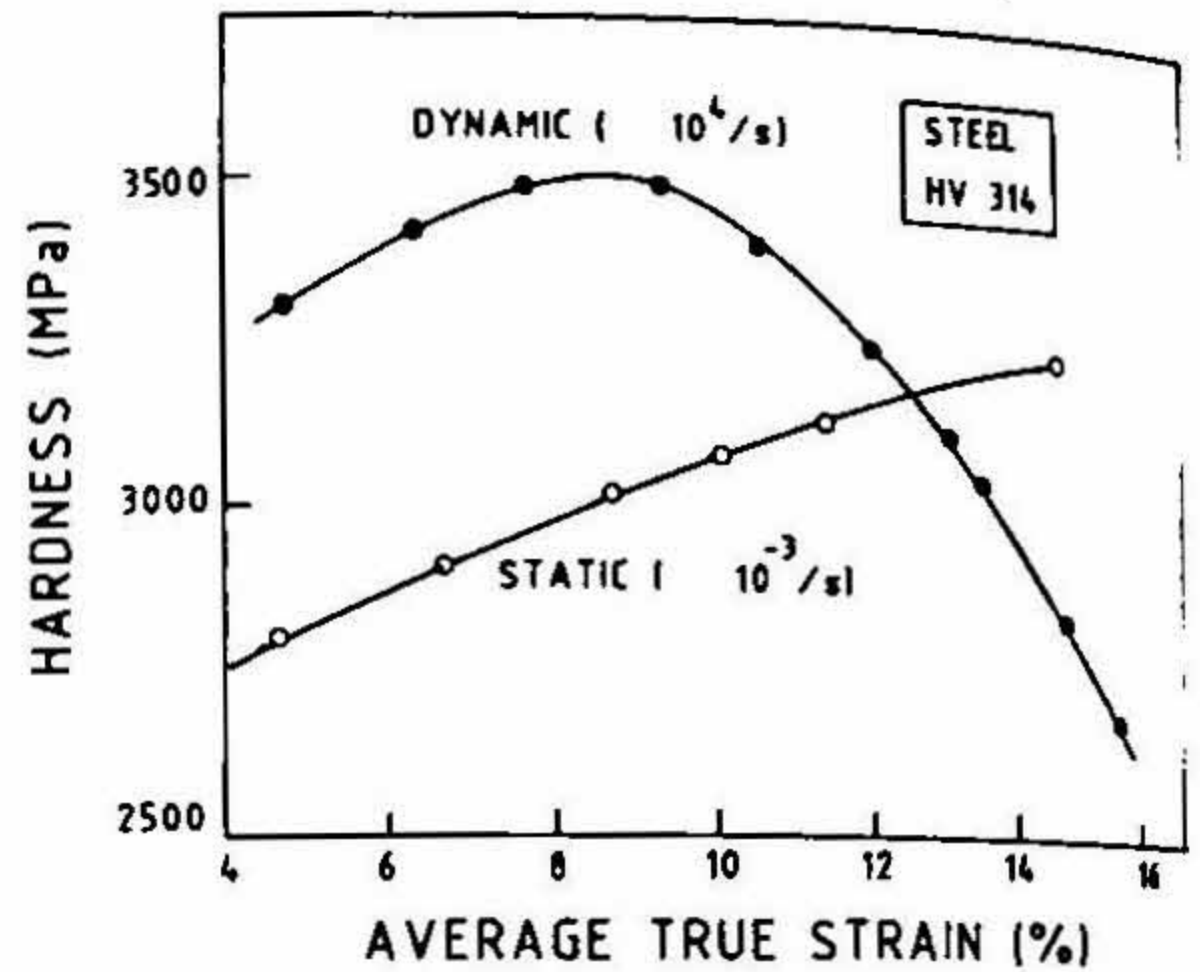FIG. 3. An eroded surface of an Al–Li alloy as seen in SEM.

FIG. 4. The variation of hardness as a function of average true strain under static and dynamic conditions.

the roughening of the surface of the component. Such a roughening is sufficient to dramatically downgrade the performance of gas turbine engines[5,6].

The above discussion points to the fact that under erosion conditions, the plastic deformation is essentially limited by the formation and extrusion of the lip since, once the lips form, they get removed as erosion debri. Thus, an estimation of limiting MED appropriate to erosion requires a knowledge of the critical plastic strain for the formation of the lip under plastic deformation conditions experienced during erosion. In the following sections, the nature of plastic deformation during erosion is first presented and is followed by the estimation of critical strain for lip formation.

Under conditions of erosion, the strain rates associated with the plastic deformation of the eroding material lie[7,8] in the range 10^4–107 s^{-1}. In addition, as in the case of a hardness test, the plastic deformation is confined to near surface regions of the component surface and occurs under constrained conditions, *i.e.*, in the presence of a substantial hydrostatic compression[9]. The above two factors also cause the deformation to be fully adiabatic[10]. Thus, erosion involves material deformation under ultra-high strain rate, constrained and adiabatic conditions.

The plastic deformation behaviour of metallic materials under such unique deformation conditions can be expected to be vastly different from that observed during a conventional tensile test characterised by low strain rate, unconstrained and isothermal test conditions. A test technique to characterize the plastic flow behaviour of metallic materials under such unique conditions is the dynamic indentation (DI) test, details of which are available elsewhere[11]. In this technique, the constrained, adiabatic and high strain rate ($\overset{\circ}{\epsilon}$ =strain rate $\simeq 10^4$s^{-1}) plastic flow behaviour of a material is obtained by impacting the material with tungsten carbide balls over a range of impact velocities (20 to 200 m/s) using a gas gun. In Fig. 4, the dynamic flow curve obtained using the DI test in the case of low alloy steel (hardness (HV) = 314) is presented and compared with the static curve obtained from conventional tests like tensile or Brinell hardness test. In this figure, the hardness

(dynamic or static) of HV314 steel is plotted against average true strain. As is known[12–14], hardness is higher than the tensile flow stress (at the same strain) by a factor of 3. The factor 3 is called the constraint factor.

The interesting features that can be observed from Fig. 4 are as follows:

(a) At low strains (< 8%), the dynamic hardness is substantially higher than the static hardness. This increase is largely due to the fact that the dynamic strain rates are about 7 orders of magnitude higher than the static strain rates and that metallic materials generally exhibit a positive strain rate hardening tendency.

(b) Beyond a strain of 10%, the dynamic hardness decreases with increasing strain and in fact becomes even lower than the static hardness in value. This unusual behaviour is the reflection of the fact that the material underneath the indenting ball undergoes localization of plastic flow (as will be shown below).

In Fig. 5, the hardness–strain curves for a hypothetical material under various assumed conditions are presented. The static and the actual dynamic curves are identical to the curves presented in Fig. 4. The isothermal dynamic curve presumes deformation to be isothermal and represents the hardness–strain curve for a material which does not exhibit plastic flow localization during dynamic indentation. Instead, if the deformation is assumed to be adiabatic, the adiabatic dynamic curve shown in Fig. 5 becomes valid. Flow stress softening induced by adiabatic heating cannot account for the dramatic decrease in hardness beyond a critical strain, as observed experimentally (Fig. 4). Thus, the ususual shape of the dynamic hardness–strain curve (Figs 4 and 5) is a manifestation of some other phenomenon which is the localization of plastic flow.
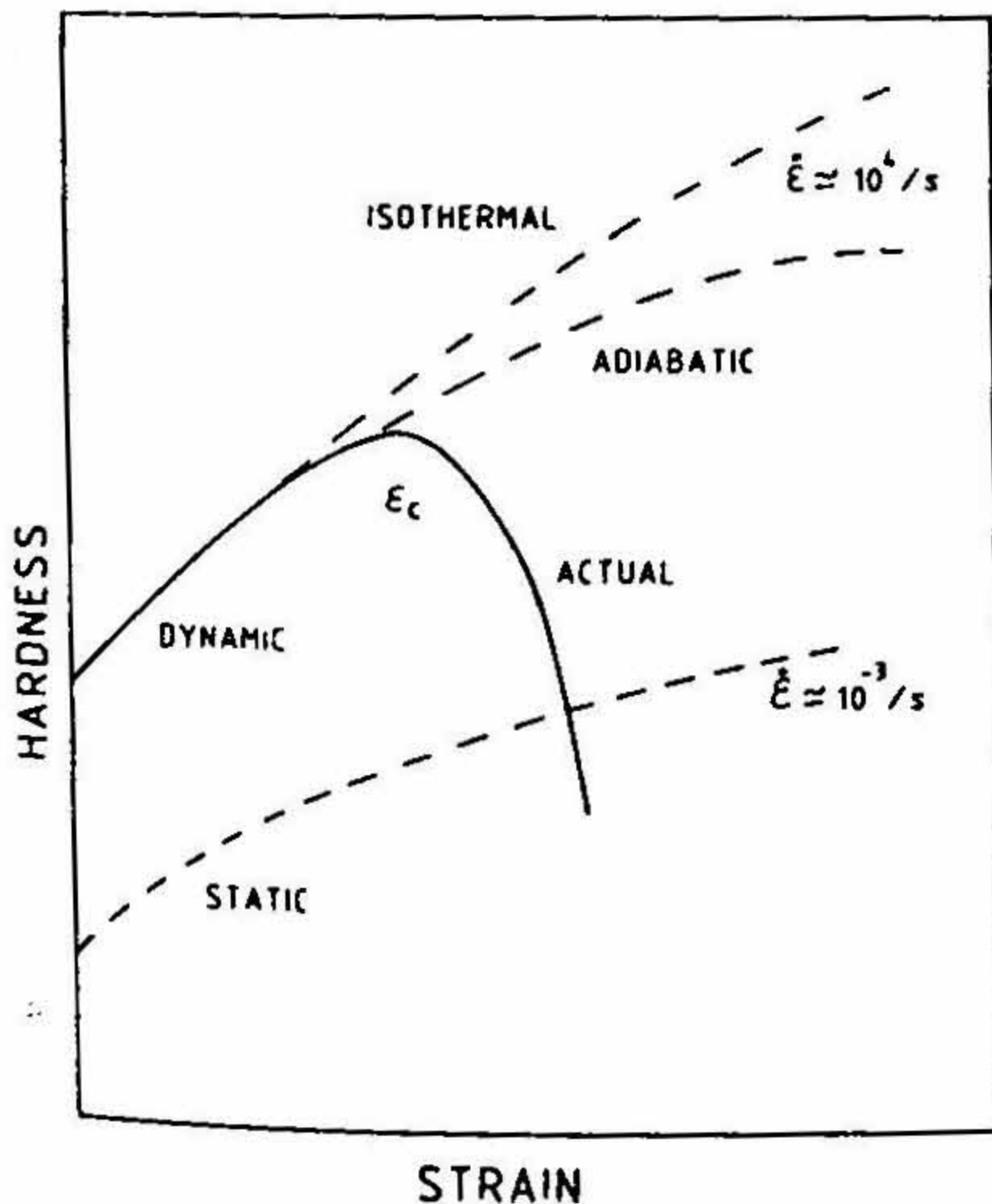

FIG. 5. Schematic diagram illustrating the variation of hardness as a function of strain under various assumed conditions.

The concept of localization of plastic flow is explained using Fig. 6. In this figure, the nature of subsurface deformation underneath the impacting particle is illustrated for (a) strain hardening, (b) perfectly plastic, and (c) strain hardening–softening material. In the case of the particle impacting a material having a high and positive strain-hardening capacity (i.e., $d\sigma / d\varepsilon > 0$, σ = flow stress, ε = true plastic strain), the plastic deformation beneath the particle spreads uniformly over a large volume, as illustrated in Fig. 6a, since it is energetically favourable. In contrast, if the particle impacts a material which has no ability to strain or work harden (i.e., $d\sigma/d\varepsilon = 0$), the deformation underneath the particle is immediately localized to the near-surface layers leading to lip formation (Fig. 6b). Figure 6c represents a more realistic case where the material exhibits a net strain hardening capacity at low strains and a net strain softening behaviour at higher strains. As shown elsewhere[11], the temperature rise in the deforming material, caused by plastic deformation at the high strain rates relevent to erosion, is responsible for such an unusual stress–strain behaviour. Under such a condition, the material deforms homogeneously up to a critical strain at which $d\sigma/d\varepsilon = 0$. At strains higher than the critical strain, $d\sigma / d\varepsilon$ is less than zero and hence the plastic deformation localizes to form a lip (Fig. 6c). The critical strain therefore represents the strain beyond which lip formation, induced by localization of plastic deformation, is promoted.

The condition for the localization of plastic flow, elucidated above, can be expressed as

$$d\sigma = (\partial\sigma / \partial\varepsilon)_{\dot{\varepsilon},T} \, d\varepsilon + (\partial\sigma / \partial T)_{\dot{\varepsilon},\varepsilon} \, dT = 0. \tag{1}$$

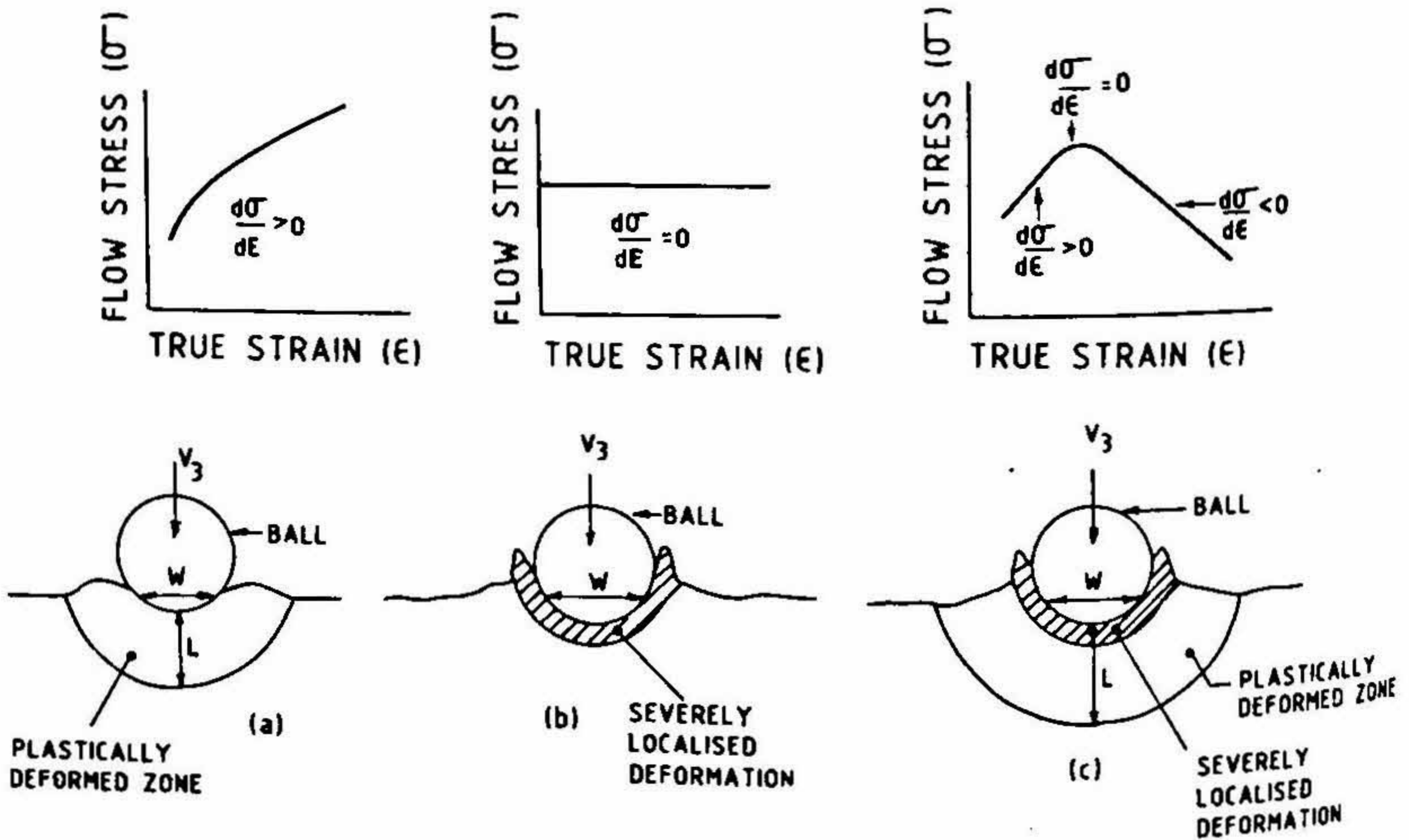

FIG. 6. Schematic representation of localisation of deformation for various types of plastic flow behaviour at high strain rates.

In eqn. 1, σ represents the flow stress, T, the temperature in K. $\partial\sigma/\partial\varepsilon$ represents the strain-hardening component and $\partial\sigma/\partial T$ corresponds to the thermal softening component. Further, a constitutive equation for plastic flow of the form,

$$\sigma_d = K_d\varepsilon^{n_d}(1 - CT) \tag{2}$$

is assumed wherein σ_d is the dynamic flow stress, K_d, the dynamic strength coefficient, n_d, the dynamic strain-hardening exponent and C, the temperature coefficient of flow stress. Substitution of eqn 2 in eqn 1 and further rearrangement gives the following expression for the critical strain (ε_c) for localization of plastic flow.

$$\varepsilon_c = [n_d\rho\, C_p / K_d C]^{1/n_d+1}. \tag{3}$$

In eqn 3, ρ and C_p are the density and specific heat, respectively, of the eroding material. Utilizing the typical values of the various parameters that enter eqn 3, the critical strain for localisation for a number of metals and alloys (Fig. 7) has been estimated[8,15]. The interesting aspect of Fig. 7 is that the critical strain for localization (ε_c) decreases with increasing strength of the metallic material. On the basis of Fig. 7, the dynamic hardness (H_d)–strain (ε) curves for two hypothetical materials, one having low K_d and high n_d (Material 1) and the other having high K_d and low n_d (Material 2) can be compared as illustrated in Fig. 8. In this figure, the area under the curves represents the MED under
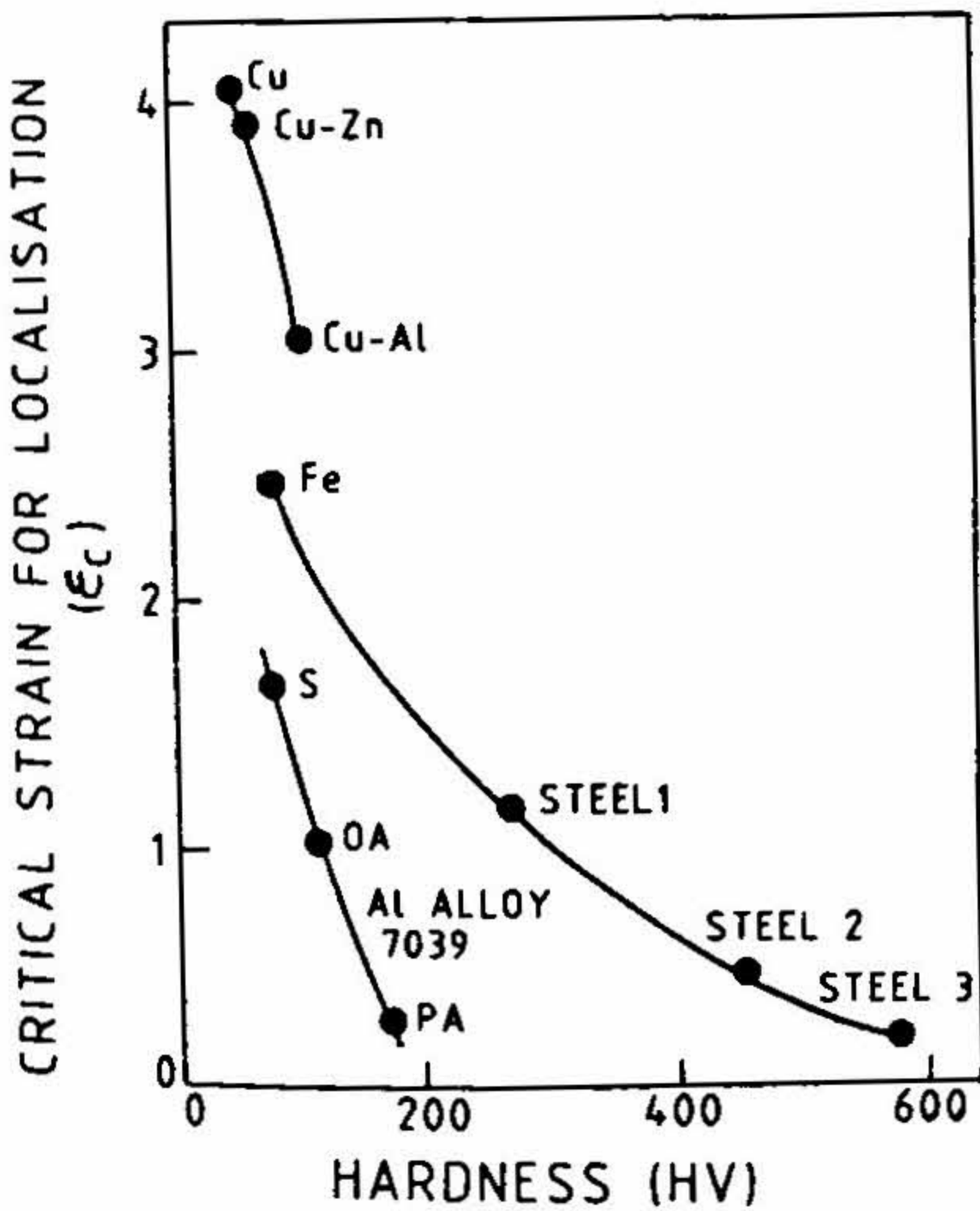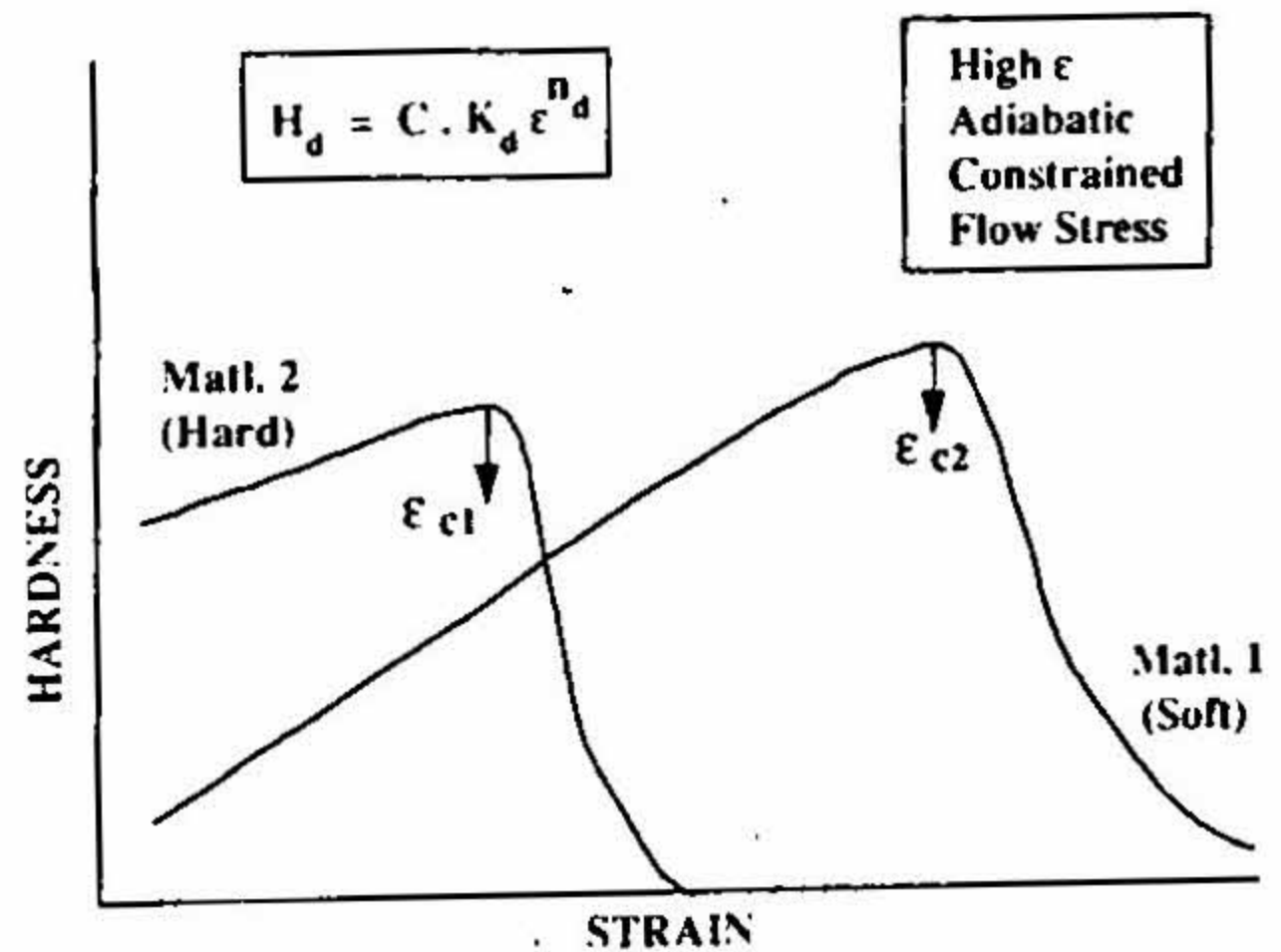

FIG. 7. The variation of critical strain for localization as a function of hardness for different materials. (In the case of Al7039 alloy S, PA and OA stand for solution treated, peak- and overaged conditions, respectively).

Matl. 1: Low K_d, high n_d. → high ε_c —soft;

Matl. 2: High K_d, low n_d. → high ε_c — hard.

FIG. 8. Schematic of the variation of hardness with strain for soft and hard materials.

Table I
Erosion resistance *versus* tensile ductility and fracture toughness

Material	Fracture toughness K_{IC} or K_{JC} MPa$\sqrt{m}$	Tensile ductility (ε_f,%)	Erosion resistance
Copper	>100	43	Highest
Cu–20Zn	–	50	Medium
Cu–5.3Al	–	66	Lowest
304 SS	290	53	Low
316 SS	206	45	Low
410 SS	160	6	Highest
Cp Titanium	>100	29	Medium
Ti–6Al–4V	83	11	Lowest
Ti$_3$Al Alloy	27	6	Highest

high strain rate, adiabatic and constrained deformation conditions appropriate to erosion. Because the critical strain for localization (ε_c) is larger for the softer material (Material 1), the MED (appropriate to erosion) is actually larger for Material 1. What this means is that *higher* hardness, or strength (the properties that are popularly used), give rise to lower MED in the material for mechanical environment and behaviour appropriate to erosion.

Now the limiting MED under erosion conditions can be computed as,

$$MED(erosion) = \int_0^{\varepsilon_c} \sigma_d \, d\varepsilon = \frac{K_d \varepsilon_c^{n_d+1}}{n_d + 1} \tag{4}$$

as opposed to limiting MED from a tensile test given by
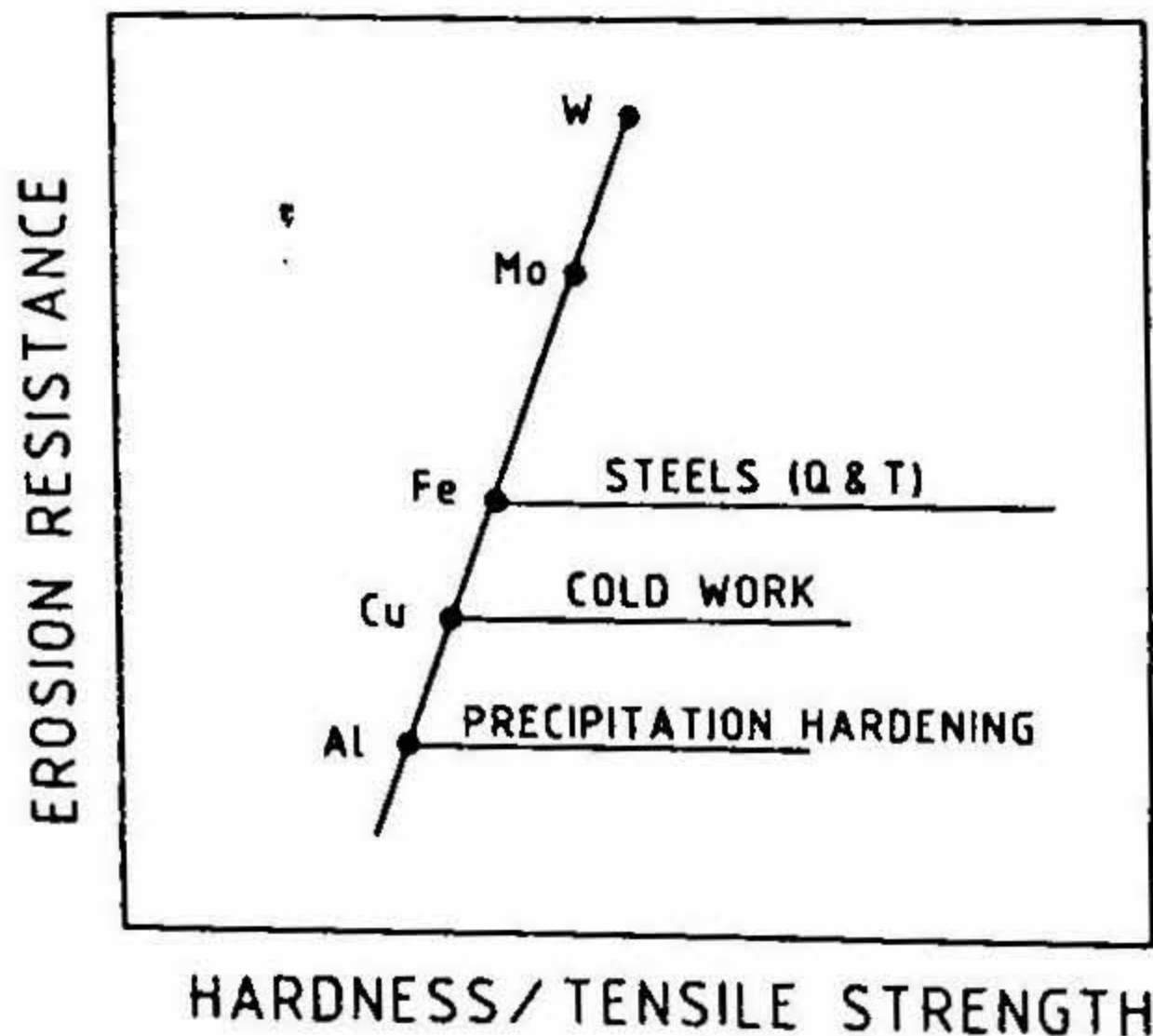

HARDNESS/ TENSILE STRENGTH

FIG. 9. The variation of the erosion resistance with hardness/tensile strength for different materials (Q- and T-quenched and tempered).

Table II
Erosion resistance *versus* harness, tensile and erosion MED

Material	Hardness (HV)	Tensile MED(MPa)	Erosion MED(MPa)	Erosion resistance
Cu	46	95	2320	Best
Cu–Zn	56	137	1367	Medium
Cu–Al	78	257	1250	Worst
Ni	100	104	1624	Medium
Ni–20Cr	193	188	1752	Best
MA 754	323	208	600	Worst
Iron	80	115	1130	Best
Steel 1	260	170	860	Medium
Steel 2	425	200	320	Worst
Steel 3	571	231	304	Worst

$$MED(tensile) = \int_{o}^{\varepsilon_f} \sigma d\varepsilon = \frac{K\varepsilon_f^{n+1}}{n+1} \tag{5}$$

where ε_f is the tensile ductility.

In Fig. 9, the erosion resistance data of a number of metals and their alloys as a function of their hardness (or strength) are presented[16]. In the case of pure metals, the erosion resistance appears to increase linearly with increasing hardness. However, in the case of alloys (*e.g.*, steels, precipitation-hardened alloys), the erosion resistance does not improve, as compared to the pure metal, even though the hardness has been raised by a factor of two to three. Similarly, as indicated in Table I, the erosion resistance has no correlation with tensile ductility or the fracture toughness.

The erosion resistance of several metals and alloys has been compared in Table II on the basis of their hardness (HV), tensile MED and erosion MED values. From Tables I and II it is clear that erosion resistance of metallic materials (as presented in Fig. 9) does not correlate with the tensile strength, hardness, tensile ductility, fracture toughness or tensile MED. In contrast, the erosion MED scales in the same manner as erosion resistance (Table II).

3. Ballistic penetration

Armours are materials used to protect tanks, equipment and personnel. A potent and common mode of attack is through the use of kinetic energy projectiles. The effectiveness of these projectiles in penetrating the armour material is dependent on their kinetic energy at the time of impact and also their integrity. From the point of view of the armour designer, the armour material should have the maximum capability to absorb and dissipate energy under ballistic penetration conditions.

Figure 10 shows in a schematic fashion the manner in which the armour material responds to the penetrating projectile. Two modes of penetration are common when the armour is a metallic material. In the first mode, called bulging, the armour material plate deforms extensively to the extent of bulging on its rear side before allowing the projectile
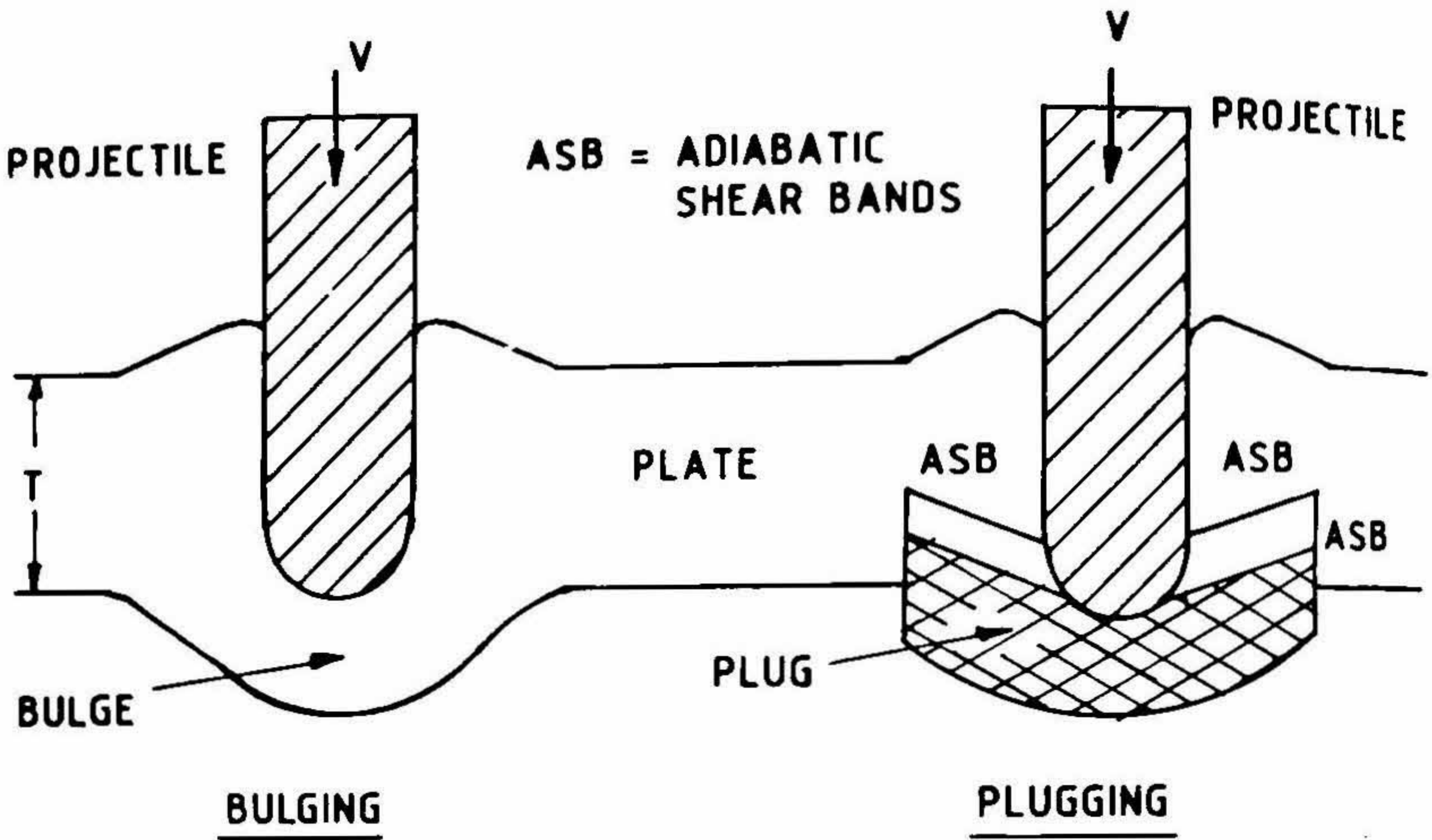
FIG. 10. Schematic representation of bulging and plugging as observed during the ballistic penetration.

to perforate. In the second mode, called plugging, the penetrating projectile initiates the formation of localised shear bands called the adiabatic shear bands (ASBs). These ASBs travel faster than the projectile and upon impinging on the rear face of the armour plate cause a plug to be removed. Once the plug forms, perforation is immediate. As illustrated in Fig. 11[17], plugging is more common in the case of armour steels with high hardness (HV > 400) while bulging is the predominant mode in the case of low hardness armour plates.
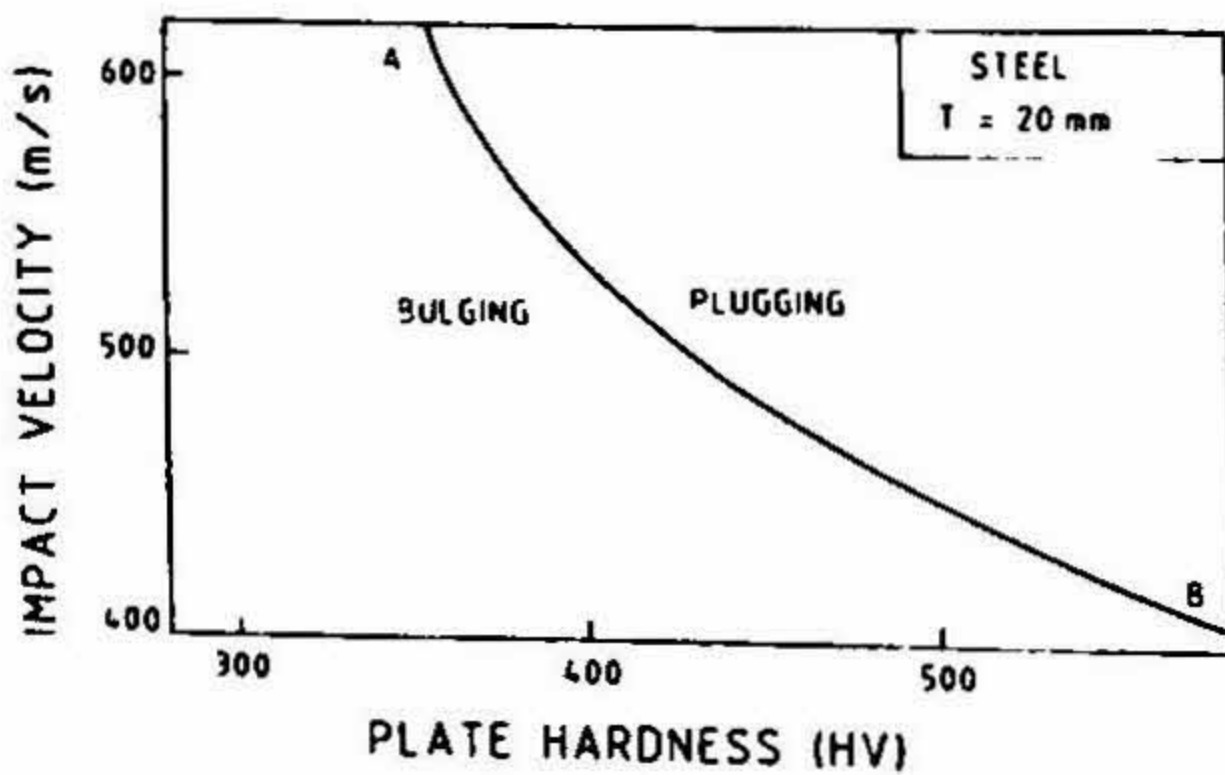

FIG. 11. The regimes of bulging and plugging at various impact velocities and plate hardness for a steel plate of 20 mm.
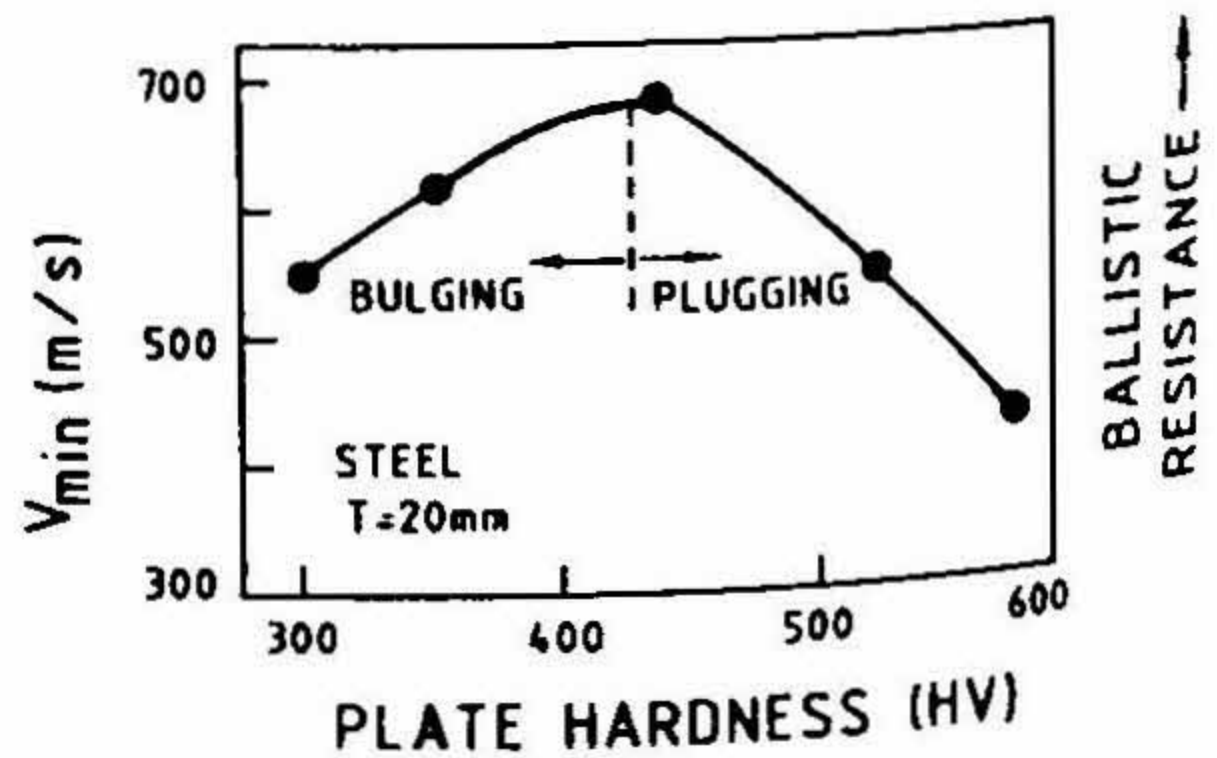
FIG. 12. The variation of the minimum velocity (V_{min}) as a function of plate hardness for bulging and plugging.
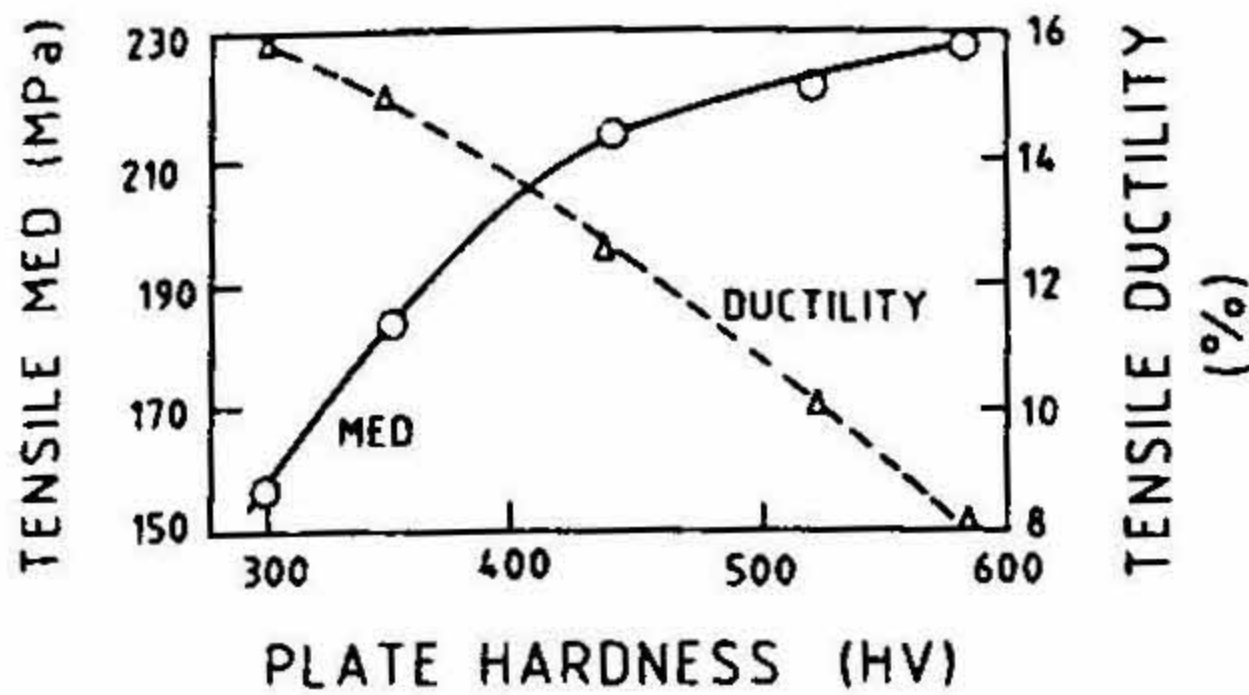
FIG. 13. The variation of the tensile MED and the tensile ductility as a function of plate hardness for a steel plate of 20 mm thickness.
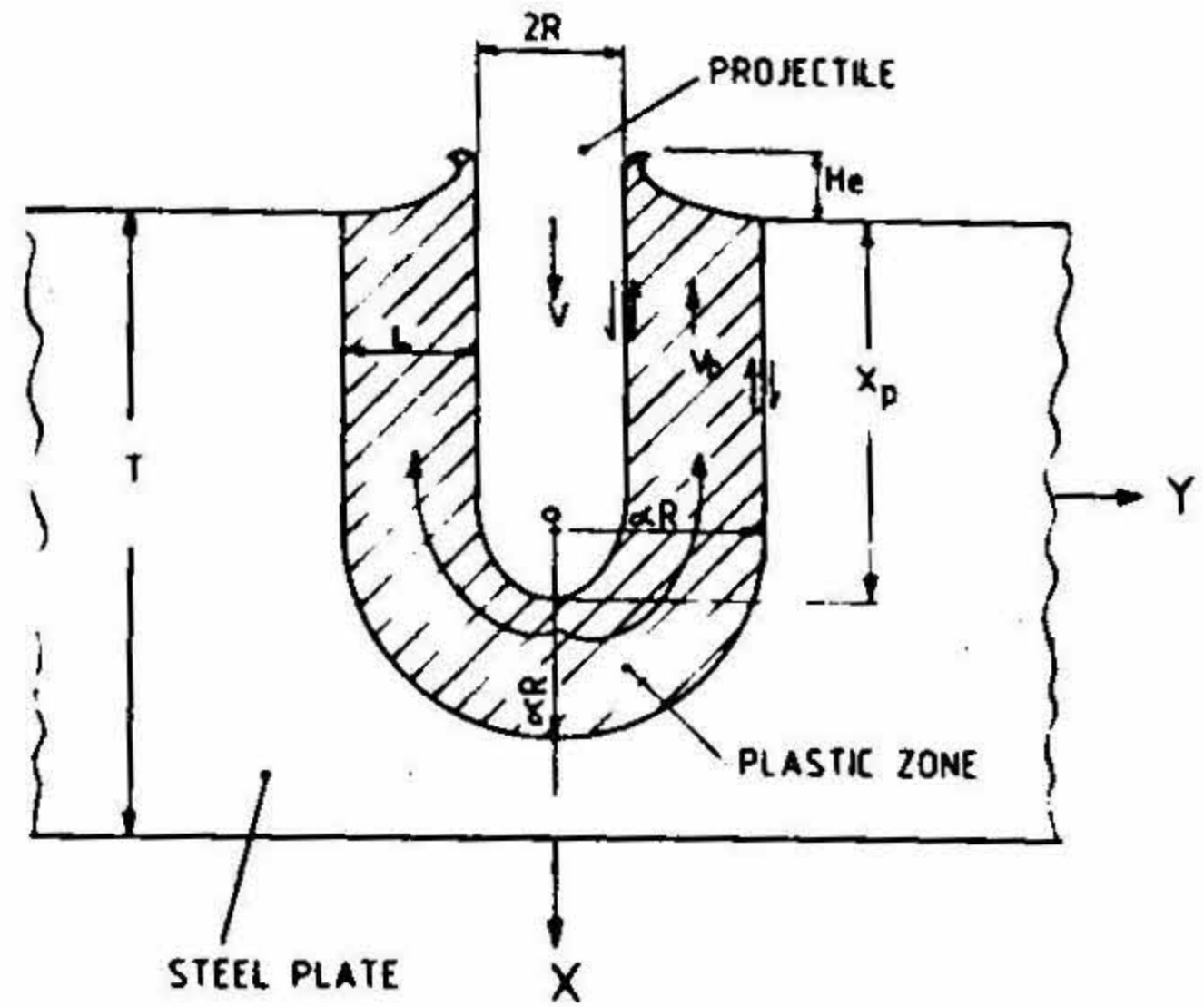
FIG. 14. Schematic representation of plastic zone around the impact crater as obtained during projectile penetration.

Among the bulging and plugging modes, the bulging mode allows for greater energy absorption and hence is preferred. The ballistic resistance of steel (defined in terms of the minimum velocity, V_{min}, at which the plate is just perforated), as a function of its hardness, goes through a maximum as illustrated in Fig. 12. Beyond the hardness of about HV 430 (in this particular example), the ballistic resistance comes down because of onset of plugging. For steels with hardness less than HV 430, bulging is the mode of penetration and, in this regime, the ballistic resistance increases with increasing hardness.

In Fig. 13, the variation of tensile MED and tensile ductility are plotted for the same steel (as in Fig. 12) as a function of plate hardness. It is clear that neither the tensile MED nor the tensile ductility predict a maximum in the ballistic resistance at intermediate hardness.

The MED appropriate to ballistic penetration can be estimated as[17,18],

$$MED(ballistic) = 0.5mV^2/U_d . \qquad (6)$$

In the above equation, m is the mass of the projectile, V, its velocity and U_d, the volume of the plastic zone formed around the projectile. The manner in which U_d is estimated is indicated in Fig. 14. The plate, penetrated by the projectile, is sectioned vertically across the crater and the plastic zone size (αR; α = constant, R = projectile radius) is measured as shown in Fig. 14. Details regarding the various methods by which the plastic zone can be discerned are given elsewhere[17]. Once the plastic zone size (αR) is measured, the plastic zone volume is estimated as[17,18].

$$U_d = \pi\alpha^2 R^3 [X_p /R - \alpha /3]. \qquad (7)$$

In the above equation, X_p represent the depth of penetration (see Fig. 14). Using eqns 6 and 7, MED (ballistic) can then be estimated.
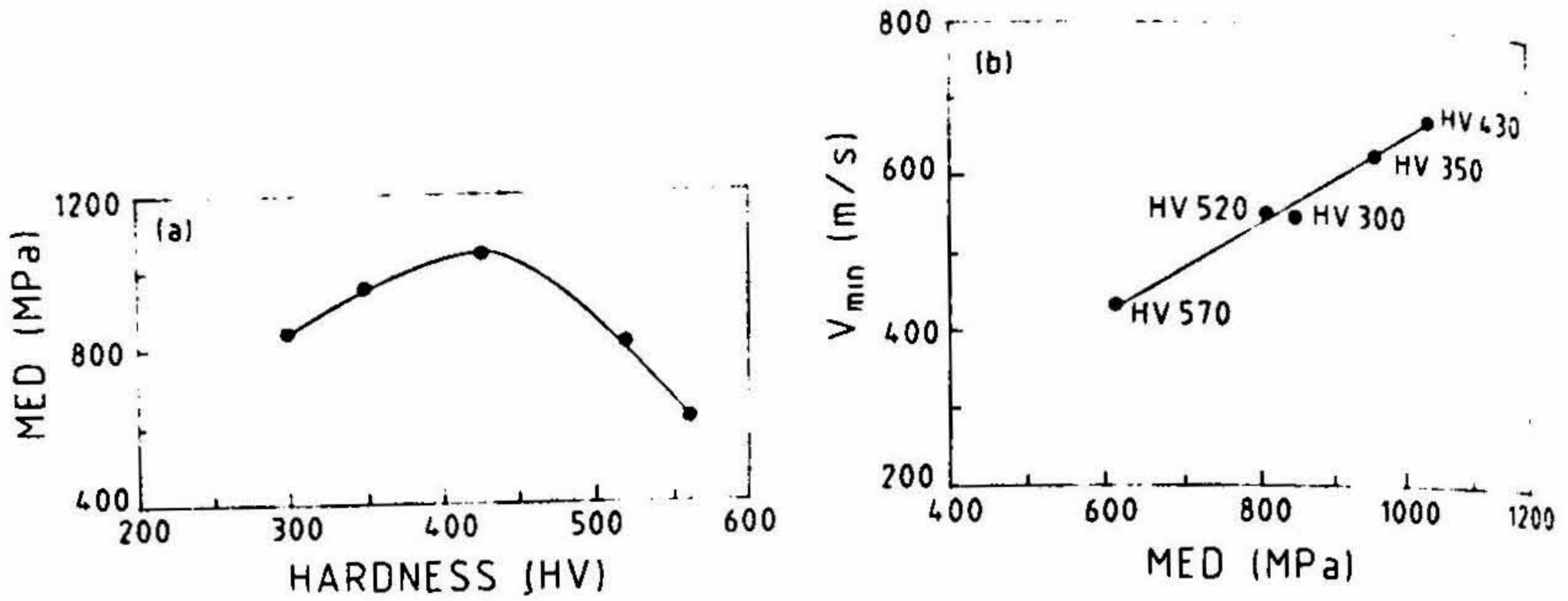
FIG. 15a. Dependence of the mechanical energy density (MED) on hardness for an armour steel. b. The variation of minimum velocity (V_{min}) as a function of the mechanical energy density (MED) for steels.

In Fig.15a, the variation of MED (ballistic) with hardness is illustrated. Unlike in the case of tensile MED or tensile ductility (Fig.13), the ballistic MED clearly goes through a maximum at intermediate hardness levels. In Fig. 15b, the variation of V_{min} (an indicator of ballistic resistance) with MED (ballistic) is presented. The correlation between ballistic resistance (V_{min}) and MED appropriate to ballistic penetration is obvious. The steel heat treated to the hardness of HV 430 exhibits the maximum MED value and also the best ballistic resistance.

4. Fatigue

A material subjected to repetitive or fluctuating stress will fail at a stress much lower than that required for failure on a single application of load. Failures under cyclic loading are termed fatigue failures. Failures occurring above about 10^4 cycles are classified as high cycle fatigue (HCF) and the stresses encountered are below the proportional limit. On the other hand, failures below 10^4 cycles are classified as low cycle fatigue (LCF) and the stresses encountered exceed the limit of proportionality and thereby involve inelastic or plastic strain.

The cycles to failure under LCF conditions are commonly analysed in terms of the applied total strain or the imposed plastic strain. It is generally observed that the LCF resistance increases with increasing tensile ductility. This is illustrated with the help of data on pure aluminium[19] and Al–Li alloys[19, 20] (Fig. 16 and Table III). Pure aluminium possesses highest tensile ductility and also maximum LCF resistance. Solid solution strengthening of Al with Li leads to a decrease in both ductility and LCF resistance. Age hardening leads to a further decrease in ductility and LCF resistance. Such an analysis suggests that higher the tensile ductility, greater is the LCF resistance. However, this analysis does not take into account the strength property. Pure aluminium, though characterised by highest fatigue life, has the lowest strength and is, thereby, not suitable for load-bearing structural applications.
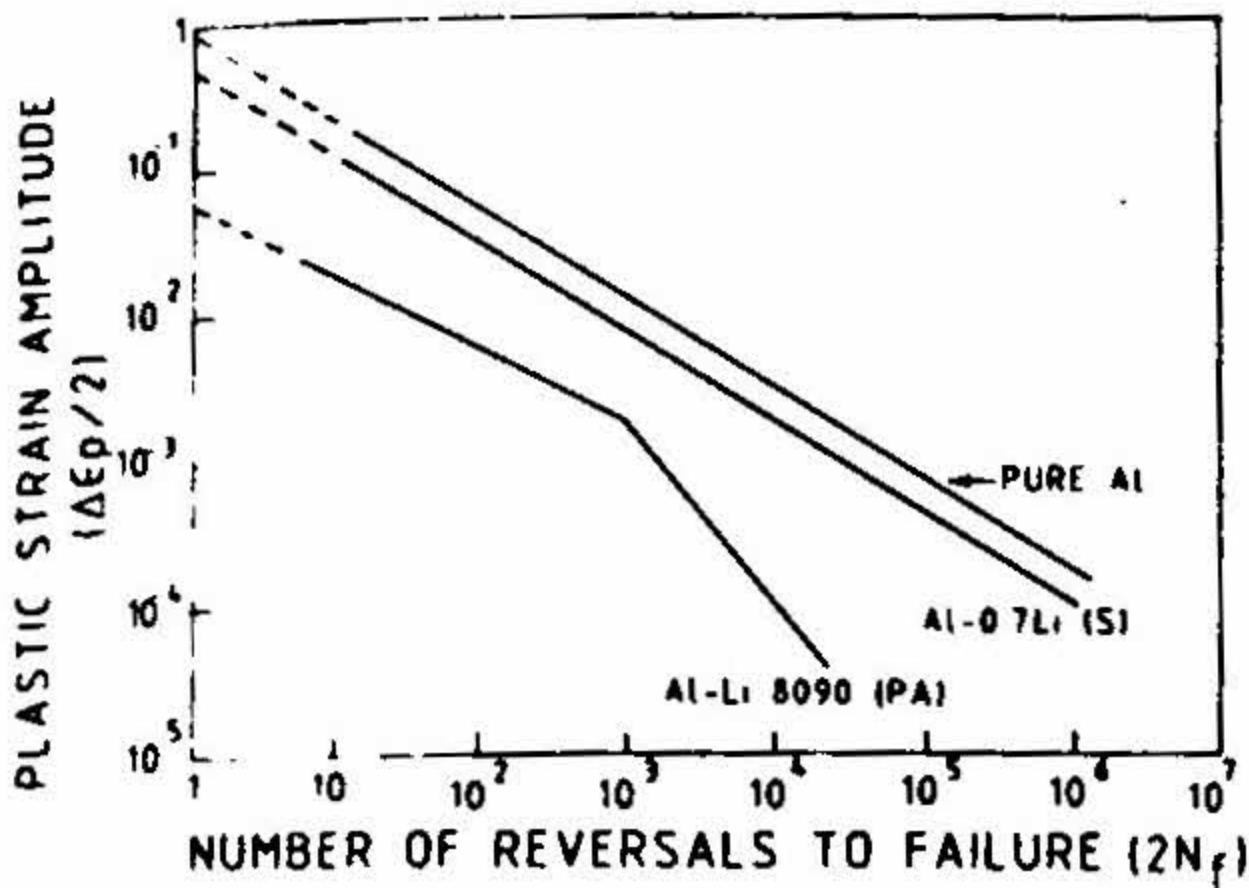
Fig. 16. Variation of $2N_f$ (number of reversals to failure) with plastic strain amplitude for pure Al (99.98% purity), Al–0.7 wt% Li (solid solution) and Al–Li 8090 (precipitation hardened; peak-aged) alloys.

The MED (fatigue), on the other hand, takes into account both strength and ductility. The MED (fatigue) is defined as the cumulative hysteretic energy till fracture. Assuming that the plastic strain energy per cycle $\Delta \overline{w}_p$; Fig. 17) is nearly constant for the entire fatigue cycling, MED is obtained as[21, 22].

$$MED(fatigue) = (\Delta \overline{W}_p)N_f$$

$$= [\int \sigma d\varepsilon_p]N_f \qquad (8)$$

where N_f is the fatigue life, σ, the stress and ε_p, the plastic strain. Assuming that the material exhibits Masing[23] behaviour, MED is computed as,

$$MED(fatigue) = \Delta \sigma \, \Delta \varepsilon_p[(1-n')/(1+n')]N_f \qquad (9)$$

where $\Delta \sigma$ is the stress range, $\Delta \varepsilon_p$, the plastic strain range (see Fig. 17) and n, the cyclic work hardening exponent in the equation $\Delta \sigma/2 = K'(\Delta \varepsilon_p/2)^{n'}$.

Fatigue life (number of reversals to failure; $2N_f$) varies as the imposed plastic strain amplitude, $\Delta \varepsilon_p/2$. For a given material, the simplest understanding can be that for smaller $\Delta \varepsilon_p$, N_f will be larger and *vice versa*, thus MED can be expected to be constant over a range of strain amplitudes and the corresponding fatigue lives. This is represented by a horizontal dotted line in Fig. 18.

Table III

Tensile ductility and LCF properties of Al and Al–Li alloys

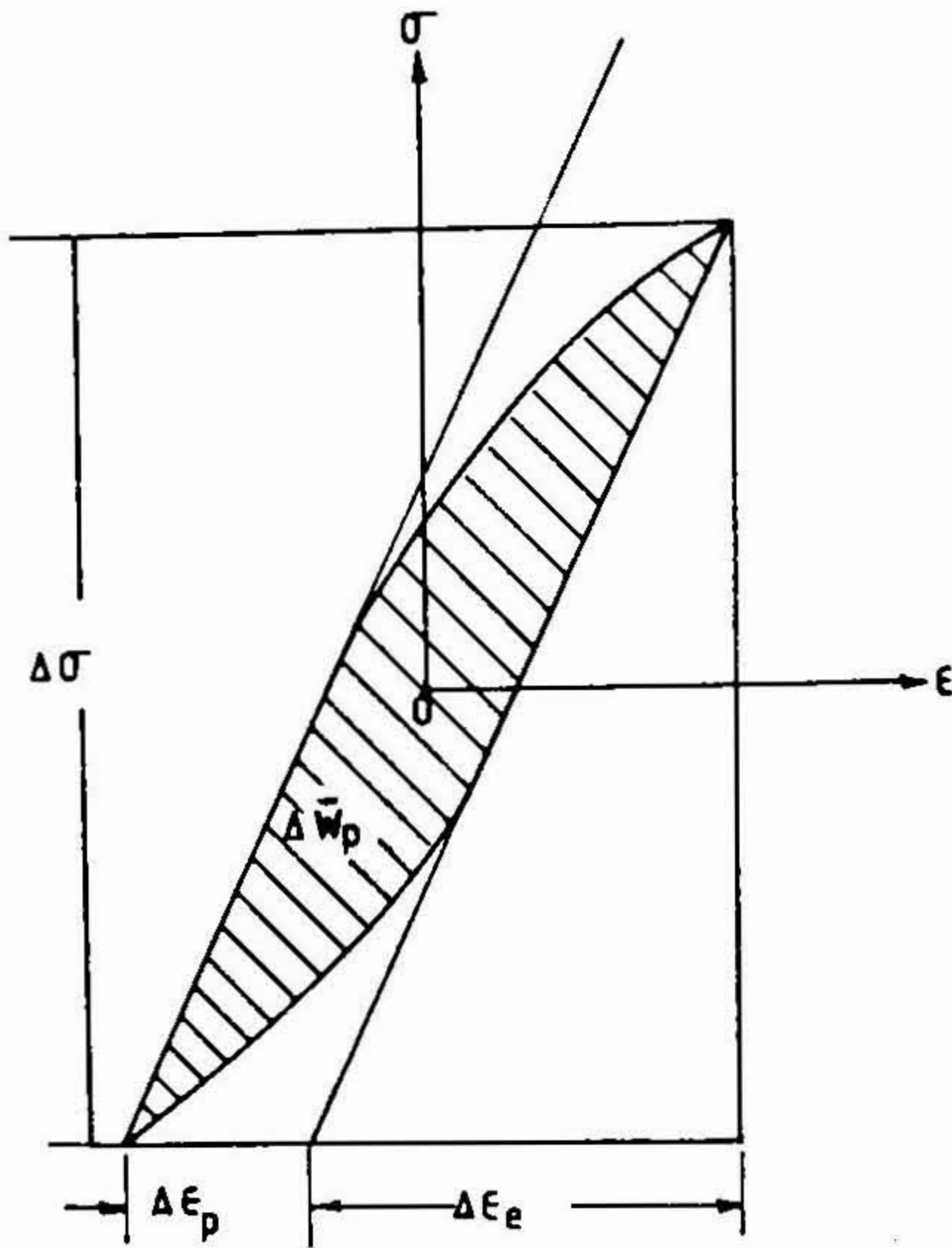| Alloy	Tensile ductility ε_f, %	Cyclic ductility coefficient ε'_f, %	N_f at $\Delta \varepsilon_p/2 = 10^{-3}$	MED(fatigue) at $N_f = 10^3$ (MJ/m³)
Pure Al	40	32	4000	680
Al–0.7Li (S: Solid solution)	26	16	3000	880
Al–Li 8090 alloy (PA:Peak aged)	5.4	5.0	2200	1300

FIG. 17. Schematic hysteresis loop showing plastic strain energy per cycle, $\Delta \overline{W}_p$.
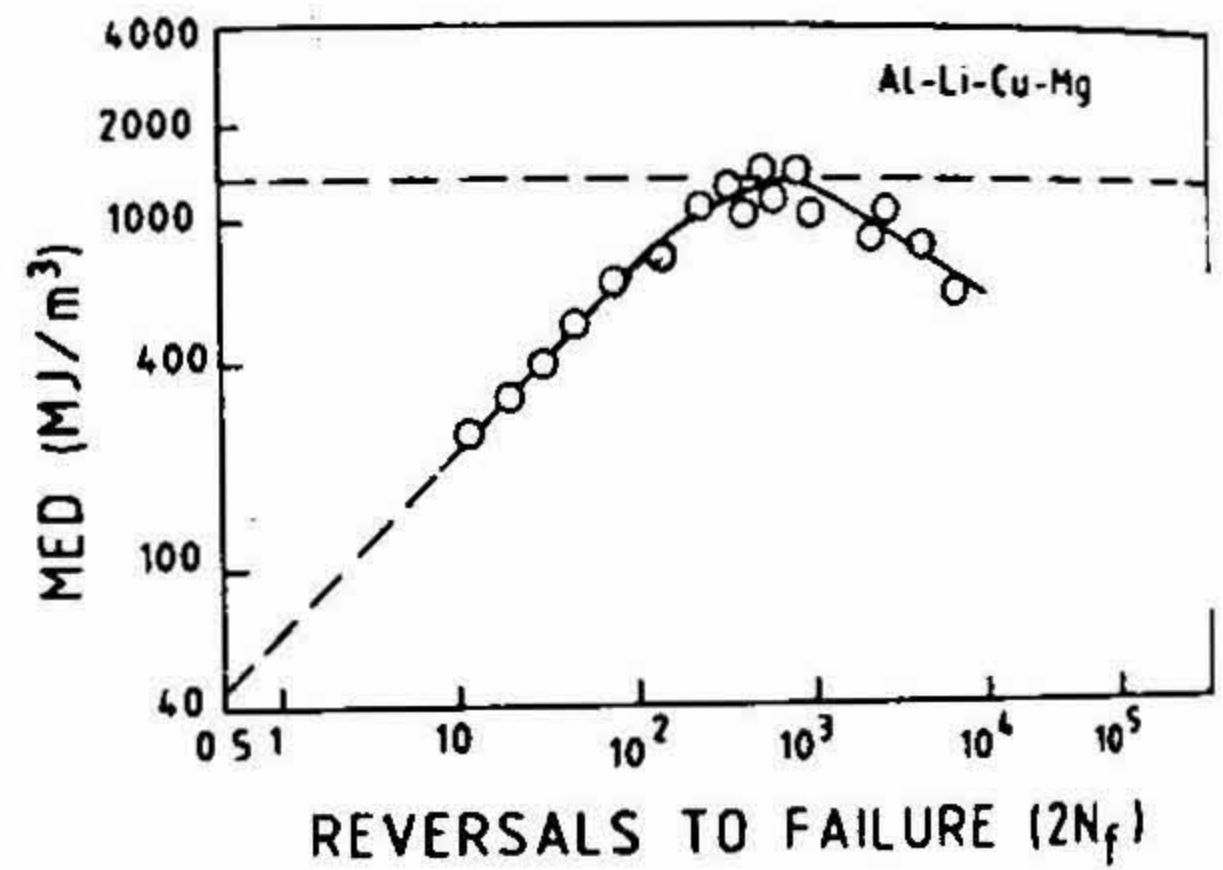

FIG. 18. Variation of MED (fatigue) as a function of fatigue life $(2N_f)$ for an Al–Li alloy 8090 in the peak-aged condition.

There are two features to be stated. First, fatigue MED (example, $\simeq 1300$ MJ/m^3 for Al–Li alloy 8090) bears no correlation with the tensile MED (31 MJ/m^3) and is more than an order magnitude greater. MED must necessarily represent a limiting value beyond which failure must occur. In view of the commonly observed trend (Fig. 18) of MED varying with strain amplitude and therefore with N_f, which will be explained subsequently, a comparison of relative fatigue resistance of different materials may be made in terms of MED corresponding to selected N_f values. This is done in Table III and it can be seen that the MED values are a satisfactory measure of relative fatigue resistance.

There is a second and an even more important feature. For instance, fatigue lives of Al–Li alloy 8090 have been observed[20] to degrade in LCF in the lower as well as higher fatigue life regions (Fig. 18). In the case of higher strain amplitude, i.e., lower fatigue life region, the degradation in LCF resistance has been attributed to strain localization. In this region, the alloy exhibits significant cyclic softening through progressive shearing of major strengthening precipitates, the ordered δ' (Al$_3$Li). The fracture mode then is lower energy ductile intergranular, as is the case under tensile loading[24, 25]. The degradation in LCF resistance in the region of higher fatigue lives (lower strain amplitudes; Fig.18) is because of quite a different cause and is attributed to a possible environmental effect. The longer test durations at lower strain amplitudes and the nature of environment present (in this case laboratory air with 30% humidity) could cause a reduction in LCF resistance. It

was found in the case of Al–Li 2020 alloy[26] that environmental degradation in LCF resistance occurs at lower strain amplitudes, but only at elevated temperatures. The present Al–Li alloy is of 8090 composition and contains relatively higher Li content (2.2–2.5 wt% as against 1.1 wt% of the 2020 alloy). Hence, Al–Li alloy 8090 could possibly be prone to environmental degradation even at ambient temperatures. Pronounced environmental degradation in fatigue crack growth studies was reported in a variety of Al–Li alloys having Li content more than 1.8 wt%, even at ambient temperatures[27,28]. It is interesting to point out that the variation of MED as depicted in Fig. 18 very well reflects these effects.

Acknowledgement

References

1. TILLY, G. P.   *Treatise on material science and technology*, 1979, Vol. 13, p. 287.

2. RUFF, A. W. AND WINDERHORN, S. M.   *Treatise on material science and technology*, 1979, Vol. 16, p. 69.

3. SAGE, W. AND TILLY, G. P.   *Aeronaut. J.*, 1969, 73, 429.

4. BITTER, J. G. A.   *Wear*, 1963, 6, 169.

5. TILLY, G. P.   *8th ICAS Congress*, Amsterdam, 1972.

6. TABAKOFF, W. AND HAMED, A.   *Proc. 6th Int. Cong. on Erosion by Liquid and Solid Impact*, Paper No. 54, 1984, Cambridge University.

7. HUTCHING, I. M.   *J. Appl. Phys.*, 1977, 10, 151.

8. MANISH ROY, TIRUPATAIAH, Y. AND SUNDARARAJAN, G.   *Mater. Sci. Engng A*, 1993, 165, 51.

9. TIRUPATAIAH, Y. AND SUNDARARAJAN, G.   *Met. Trans. A*, 1991, 22, 2375

10. SUNDARARAJAN, G.   *Wear*, 1993, 162–164, 773.

11. TIRUPATAIAH, Y. AND SUNDARARAJAN, G.   *J. Mech. Phys. Solids*, 1991, 39, 243.

12. TABOR, D.   *Rev. Phys. Tech.*, 1970, 1, 145.

13. HILL, R.   *The mathematical theory of plasticity*, 1950, Clarendon.

14. ISHLINSKY, A. J.   *J. Appl. Math. Mech.*(Engl. Transl.) 1944, 8, 233.

15. TIRUPATAIAH, Y.   Ph. D. Thesis, Banaras Hindu University, 1991.

16. SUNDARARAJAN, G.   *Scr. Metall.*, 1985, 19, 347.

17. DIXIT, S. N. AND SUNDARARAJAN, G.   *Int. J. Impact Engng*, 1992, 12, 373.

18. DIXIT, S. N., KUTUMBARAO, V. V.   *Int. J. Impact Engng*, 1995, 16, 293.
    AND SUNDARARAJAN, G.

19. DHERS, J., DRIVER, J. AND   In *Aluminium–lithium alloys III, Proc. 3rd Int. Conf. on
    FOURDEUX, A.   Aluminium–Lithium Alloys,* The Institute of Metals, London, 1986, p. 233.

20. ESWARA PRASAD, N.   *Scr. Metall. Mater.*, 1994, 30, 1497.
    PARADKAR, A. G., MALAKONDAIAH, G.
    AND KUTUMBARAO, V. V.

21. HALFORD, G. R.   *J. Mater.*, 1966, 1, 3.

22. JODEAN MORROW.   *ASTM STP* 378, ASTM, Philadelphia, 1965, p. 45.

23. MASING, G.   In *Proc Second Int. Congress on Applied Mechanics,* Zurich, Switzerland, 1926, p. 332.

24. ESWARA PRASAD, N.   In *Advances in fracture research, Proc. 7th Int. Conf. Fracture,*
    MALAKONDAIAH, G., RAJU, K. N.   (K. Salama, K. Ravichander, D. M. R. Taplin and P. Rama Rao,
    AND RAMA RAO, P.   eds), Vol. II, 1989, p. 1103, Pergamon Press.

25. ESWARA PRASAD, N.,   *Mater. Sci. Technol.*, 1995 (in press).
    MALAKONDAIAH, G.,
    KUTUMBARAO, V. V. AND
    RAMA RAO, P.

26. SRIVATSAN, T. S., YAMAGUCHI, K.   *Mater. Sci. Engng*, 1986, 83, 87.
    AND STARKE, E. A.

27. PAO, P. S., IMAM, M. A.,   *Corrosion*, 1989, 45, 530.
    COLLEY, L. A. AND YODER, G. R.

28. PIASCIK, R. S. AND GANGLOFF, R. P.   *Metall. Trans. A*, 1991, 22, 2415.